Wind tunnel validation of computational fluid dynamics-based aero-optics model

D Nahrstedt[1]*, **Y-C Hsia**[1], **E Jumper**[2], **S Gordeyev**[2], **J Ceniceros**[3], **L Weaver**[4], **L DeSandre**[5], and **T McLaughlin**[6]
[1]Boeing Directed Energy Systems, CA, USA
[2]Department of Aerospace and Mechanical Engineering, University of Notre Dame, South Bend, IN, USA
[3]Boeing SVS, Albuquerque, NM, USA
[4]Air Force Research Laboratory, AFRL/DE, Kirtland AFB, NM, USA
[5]Office of Naval Research, One Liberty Center, Arlington, VA, USA
[6]US Air Force Academy, Colorado Springs, CO, USA

The manuscript was received on 3 June 2008 and was accepted after revision for publication on 27 August 2008.

DOI: 10.1243/09544100JAERO385

Abstract: A computational fluid dynamics (CFD)-based aero-optics validation study was conducted in wind tunnel tests at the US Air Force Academy. A 12 in diameter hemisphere-on-cylinder laser turret was tested in the 3 ft × 3 ft subsonic wind tunnel at flow speeds ranging from mach 0.3 to 0.5. Flow validation was based on mean and rms velocity, mean pressure profile, rms unsteady pressure, and separation point. Optical validation was based on rms phase variance and inflow phase correlation length derived from two-dimensional Hartmann wavefront sensor data, measured over a 5 in beam. The CFD code used a two-equation turbulence model with partially-averaged Navier–Stokes approach. Good agreement was observed between measurements and predictions over line-of-sight angles ranging from 60 to 132° measured with respect to flow heading.

Keywords: adaptive optics, aerodynamics, aero-optics, wavefront sensing, wind tunnel

1 BACKGROUND

A high-energy laser on a tactical aircraft offers a variety of target opportunities and engagement advantages. Its integration and operation, however, present several challenges. Due to aerodynamics, beam director location and configuration may adversely affect the transmitted beam wavefront error (WFE), depending on line-of-sight (LOS). For the inviscid flow field about an airborne turret, the perturbations vary at a relatively slow rate (few Hertz) and are easily compensated by using adaptive optics. However, the aerodynamic-induced flow closer to the transmitter window will produce a thin turbulent boundary layer, and for LOS beyond flow separation, a free turbulent shear layer that increases in thickness with LOS angle. The separated flow is characterized by high-frequency density fluctuations that translate to optical phase errors. These are difficult to correct with current adaptive optics systems.

In the absence of expensive flight or wind tunnel testing, the accuracy of determining requirements and performance benefits of phase compensation are limited by the fidelity of the model used to determine the wavefronts corrupted by the flow. The approach in this study, defining the computational fluid dynamics (CFD)-based aero-optics model, is to use an upgraded CFD code to determine the time-dependent flow solution, for the conversion of the resulting three-dimensional density map to an optical index of refraction grid, and a path integration to determine the optical path difference (OPD) or WFE along each LOS through the index field. Until now, no CFD code described in the open literature has been validated on a one-to-one wind tunnel scale at an optical wavelength level. In the past, validation has been limited to scaling optical figures-of-merit (FOMs) and anchoring to flow properties such as pressure, velocity, and vorticity.

*Corresponding author: Boeing, Directed Energy Systems, 8531 Fallbrook Ave, MS 033-WB53, West Hills, CA 91304, USA.
email: david.a.nahrstedt@boeing.com

2 APPROACH

The approach to validating the CFD-based aero-optics model is as follows.

1. Establish flow conditions, turret scale, and required measurements.
2. Integrate the wind tunnel, flow sensors, turret, wavefront sensor (WFS), and beam relay systems. Conduct the wind tunnel tests, measuring properties of the flow fore and aft of the turret, and the wavefront properties of the transmitted beam through the flow as a function of LOS angle.
3. Model the three-dimensional flow in the wind tunnel-turret system using the CFD code by assuming the measured inlet flow. Modelling includes grid generation for the flow solution and wall effects of the tunnel.
4. Compare the OPD and phase correlation statistics between the wind tunnel measurements and CFD-based model predictions, as a function of LOS angle. Also, compare the statistics of the downrange (aft of turret) flow parameters with those based on the flow measurements.

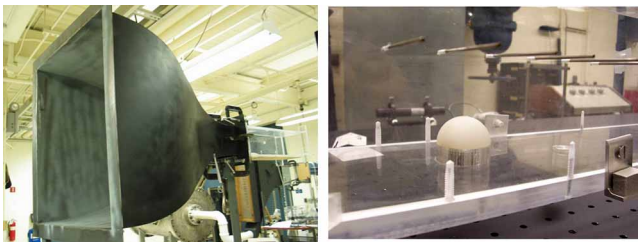

Fig. 1 Notre Dame wind tunnel inlet (left) and test section (right) for 1.5 in (3.8 cm) diameter turret tests

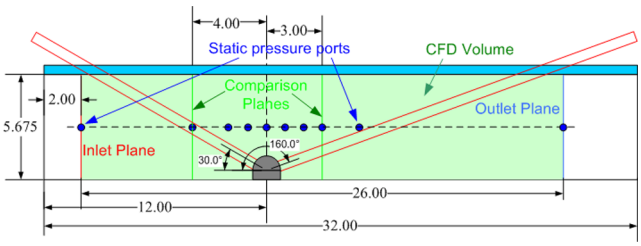

Fig. 2 Test section for 1.5 in turret measurements. Overhead LOS elevation angles range from 30 to 160° (0 = flow heading)

3 PHASE I: SUMMARY

There were two phases for the validation programme. Phase I measured the optical wavefront properties of subsonic flow over a small 1.5 in (3.8 cm) diameter turret. This provided the opportunity to verify the experiment and analysis approaches prior to validation by using the larger, more realistic 12 in (30.5 cm) diameter turret.

The 1.5 in turret with conformal window was tested at mach numbers ranging from M0.36 to M0.68, at the University of Notre Dame's subsonic wind tunnel. The tunnel inlet and test configuration, including LOS angles, are shown in Figs 1 and 2. Figures 3 and 4 show the turrets used to measure pressure and wavefront, respectively. The optical turret uses a collimated input beam to sample the flow. This reflects off a plane mirror and is relayed to the WFS. The pressure turret has

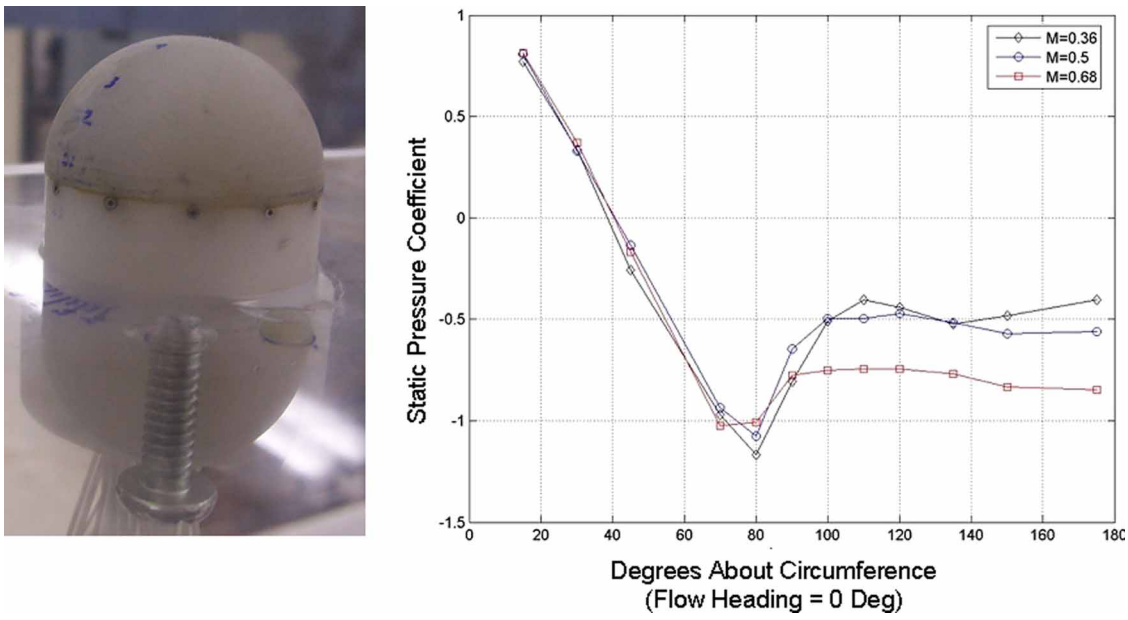

Fig. 3 Turret instrumented for flow measurements. Static pressure profile

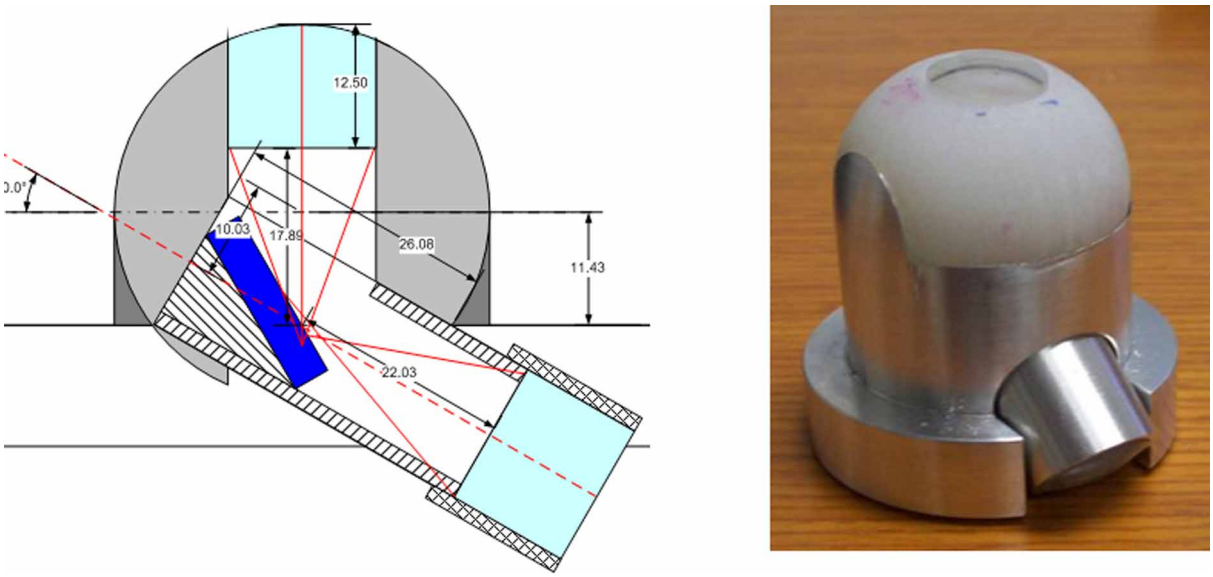

Fig. 4 Conformal window turret for optical WFS measurements (dimensions in mm)

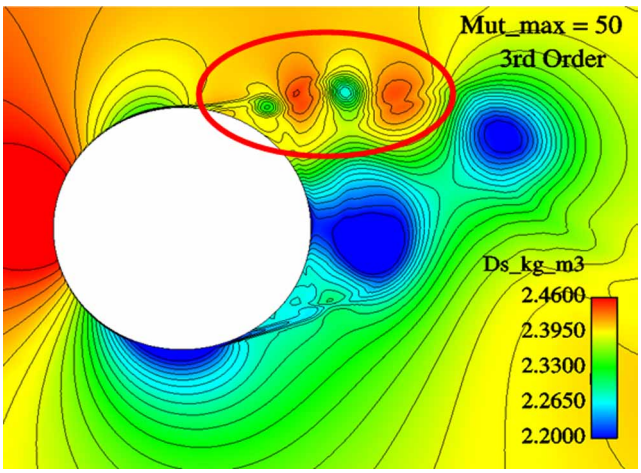

Fig. 5 CFD-based density contours showing improved resolution of vortex structure in shear layer (encircled)

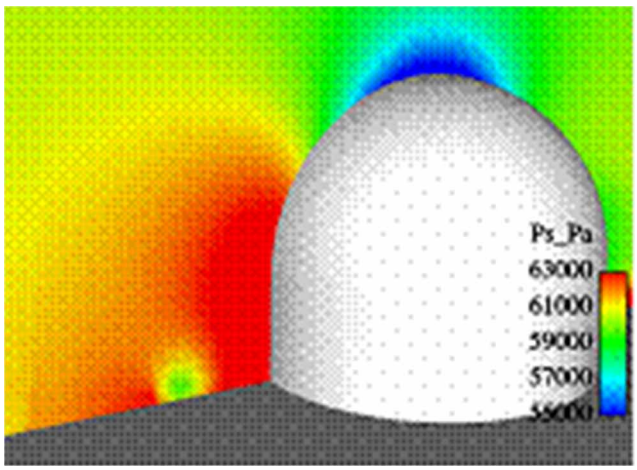

Fig. 6 Pressure contours showing increased resolution of necklace (horseshoe) vortex

several surface mounted sensors to measure static and dynamic pressure at the cylinder-hemisphere intersection, and flow velocity profile at different planes along the flow direction. Examples of the initial CFD flow solution, in Figs 5 and 6, show the areas where the model was improved by increasing computational node density and implementing the partially-averaged Navier–Stokes (PANS) model discussed below. This resulted in increased spatial resolution of the vortex structure in the shear layer (Fig. 5) and necklace vortex about the base (Fig. 6).

Figures 7 and 8 compare the rms WFE and inflow correlation length of the phase for the measured and CFD-based optical phases. The area shaded green (Fig. 7) is the range of expected rms OPD values based on a $1/\sin\theta_{\text{elev}}$ factor for optical path through a shear layer of constant thickness (lower bound) and 10° diverging shear layer combined with the $1/\sin\theta_{\text{elev}}$ factor (upper bound). Both the measured and CFD results are consistent with the scaled increase in optical path.

4 PHASE II: WIND TUNNEL FLUID AND OPTICAL MEASUREMENTS

4.1 Wind tunnel

The phase II experiments were conducted in the subsonic wind tunnel at the US Air Force Academy, Colorado Springs, CO. The tunnel has a 3 ft × 3 ft × 8 ft (0.91 m × 0.91 m × 2.44 m) test section, as shown

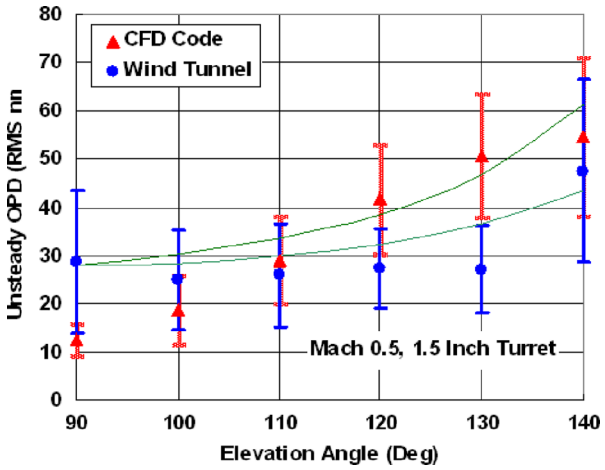

Fig. 7 Comparison of rms WFE from WFS measurements and CFD model

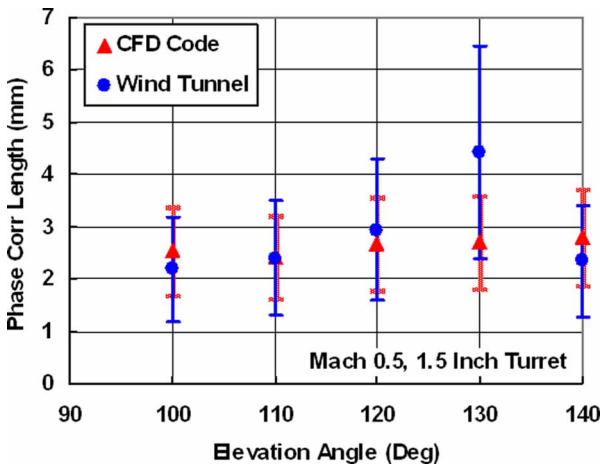

Fig. 8 Comparison of inflow phase correlation length from WFS measurements and CFD model

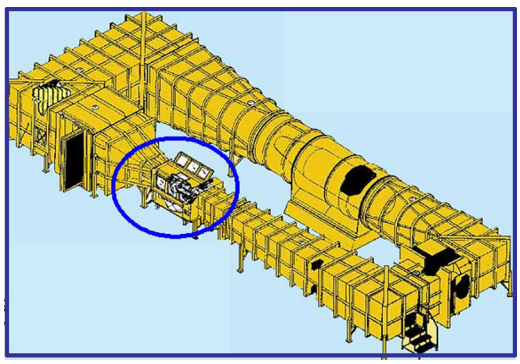

Fig. 9 Thirty-six inch (0.91 m) wind tunnel at the US Air Force Academy: test section circled

in Fig. 9. Mach numbers in the test ranged from M0.35 to M0.45.

Figure 10 shows the configuration of the larger optical turret. The turret is composed of a 12 in diameter sphere mated to a cylindrical base. The hollow sphere

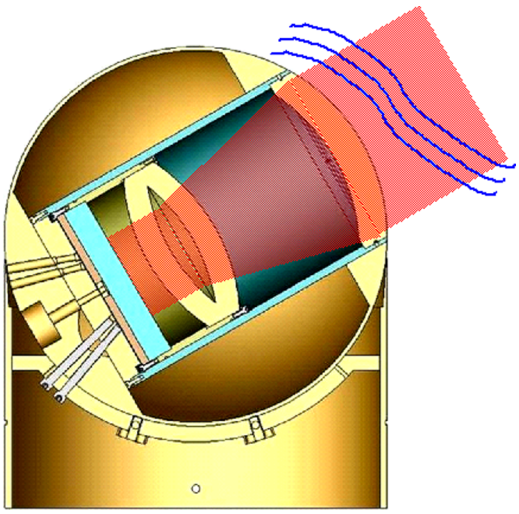

Fig. 10 Optical turret is 12 in (30.5 cm) in diameter with 5 in (12.7 cm) beam

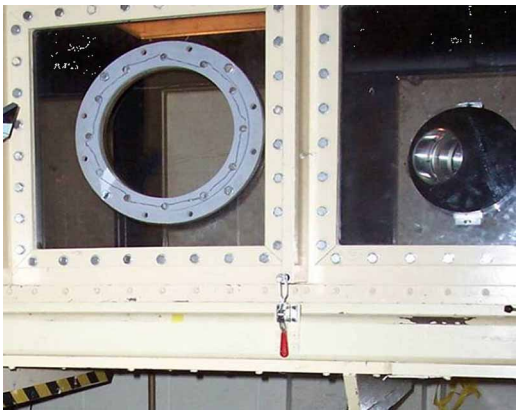

Fig. 11 Turret (at right) mounted on wind tunnel wall

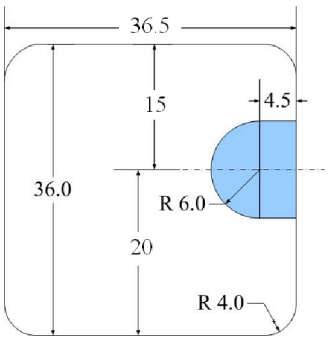

Fig. 12 Wind tunnel test section: dimensions (inches)

is fitted with a flush-mounted convex lens with outer radius of curvature matching that of the sphere. The sphere can be rotated, allowing a variation in elevation angle between 40 and 140°. The cylindrical base, sealed to a flat plate, can be rotated in azimuth angle. Sealing the base ensures that the interior of the beam director is nominally at the test-section static pressure.

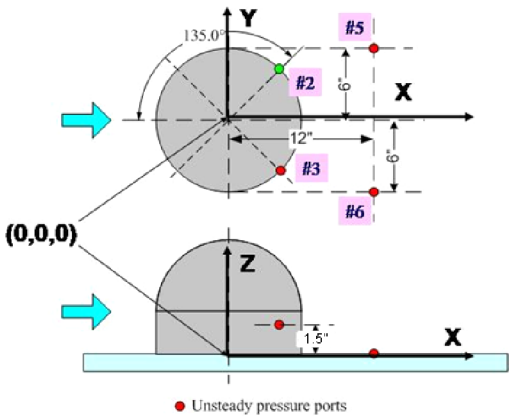

Fig. 13 Turret coordinate system and locations of unsteady pressure sensors

The turret base plate is mounted to the interior wall of the wind tunnel, as shown in Fig. 11. The turret location and test section dimensions are shown in Fig. 12. The turret is 54 in (1.37 m) downstream from the entrance to the test section.

4.2 Flow measurements

Figures 13 and 14 show the turret coordinate system defining the location of the pressure and velocity sensors. The turret has ten static pressure ports and four Kulite unsteady pressure sensors (two mounted on the turret and two on the mounting plate downstream of the turret). The Kulite sample rate was 100 kHz, with a low-pass filter cut-off at 40 kHz to reduce noise. Profiles of the streamwise velocity in the direction normal to the mounting plate (z-direction) were measured. Figure 14 shows the velocity profile of the incoming boundary layer upstream of the turret at sensor no. 1 location. The thickness of the boundary layer is ~2 to 2.5 cm. This is consistent with boundary layer measurements conducted in the wind tunnel by using a static pressure rake [**1**].

4.3 Optical measurements

Two-dimensional wavefronts uncorrelated in time (10 Hz) were measured by using a Wavefront Sciences' two-dimensional Hartmann WFS system. The optical configuration is shown in Fig. 15. A frequency-doubled Nd:YAG laser beam (6 ns pulse duration) was expanded to a 5 in (12.7 cm) diameter collimated beam and directed from the optical bench through the test section to the turret by using two 8 in (20.3 cm) flats. The return beam from the turret was directed to the Shack–Hartmann WFS by using a cube beamsplitter.

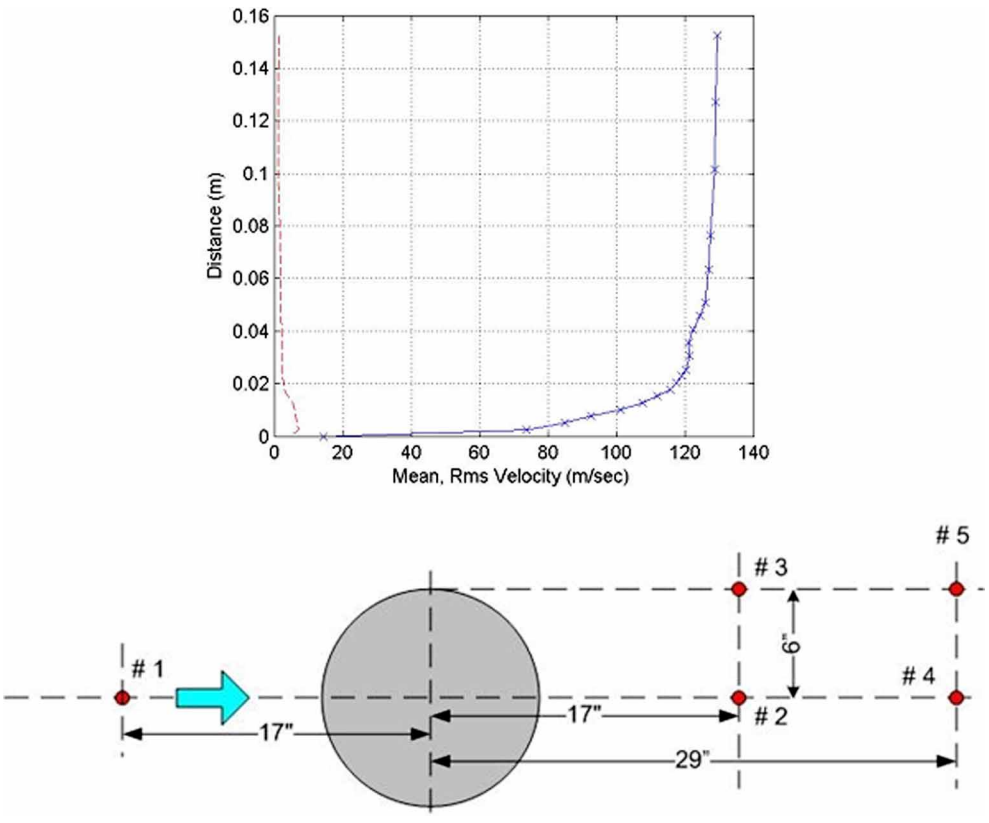

Fig. 14 Location of hot wire sensors. Plot shows mean (right) and rms (left) velocity profiles at upstream location no. 1, forward of the turret at $x = -17$ in (−43.2 cm) and $y = 0$ in

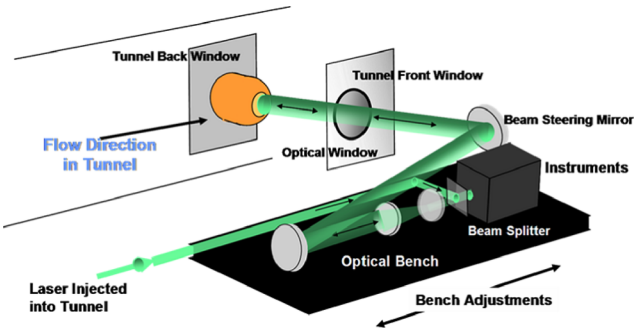

Fig. 15 Integration of Hartmann WFS with wind tunnel test section and relay optics

The WFS uses a 24 × 36 subaperture lenslet array. Two hundred wavefronts were recorded at each elevation angle and mach number. To minimize the higher-order WFE at the edge of the pupil in the beam expansion optics, only the central 4.5 in (11.4 cm) diameter was used to calculate WFE.

The Hartmann WFS data at each elevation angle and mach number were processed as follows.

1. A 'no-flow' condition wavefront was measured at the beginning of each run to characterize the static aberration. This provided a reference for evaluating the time-varying, higher-order component.
2. The mean (piston) and tip-tilt components were removed from each wavefront in the ensemble.
3. The 'steady-state' or DC phase was computed by averaging the residual wavefronts in step 2.
4. The steady-state wavefront was subtracted from each wavefront in the ensemble, and rms OPD calculated.
5. The average rms OPD for the ensemble was calculated.

Figure 16 shows some prominent flow features of the selected wavefronts measured at elevation angles of 76°, 90°, and 132°.

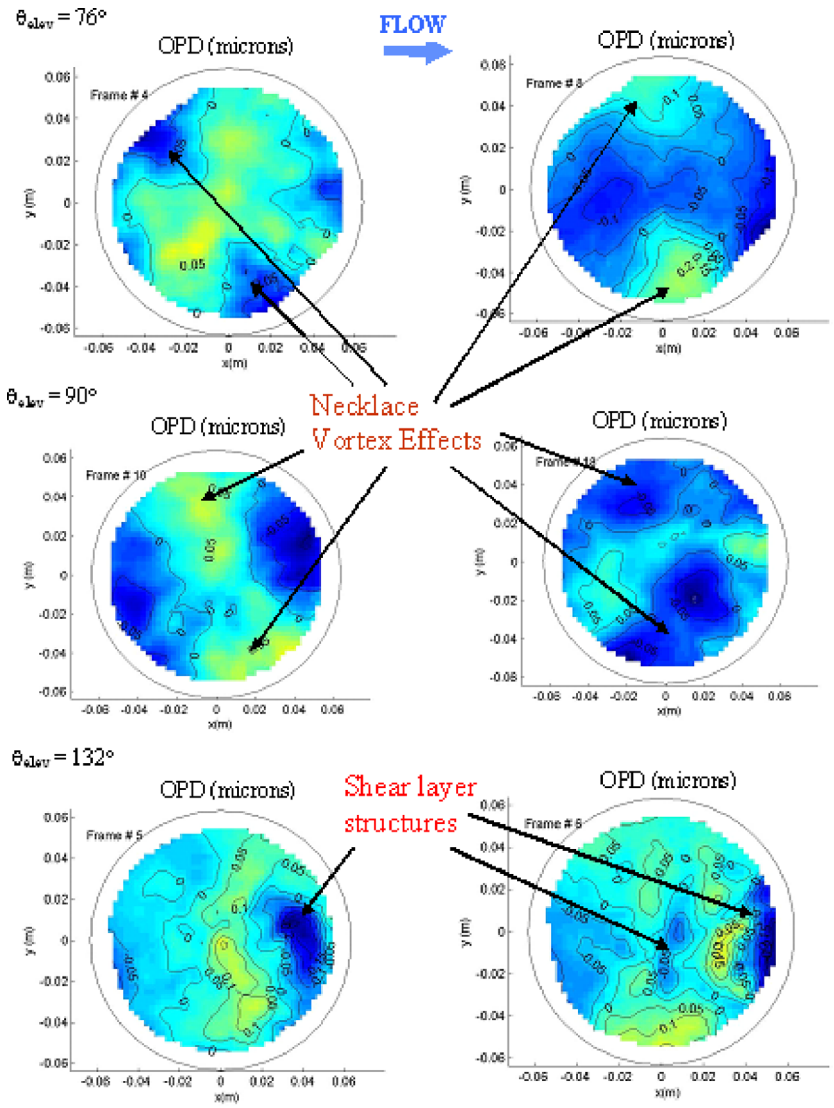

Fig. 16 Wavefront realizations at elevation angles of 7°, 9°, and 132°. M0.4 flow is left to right

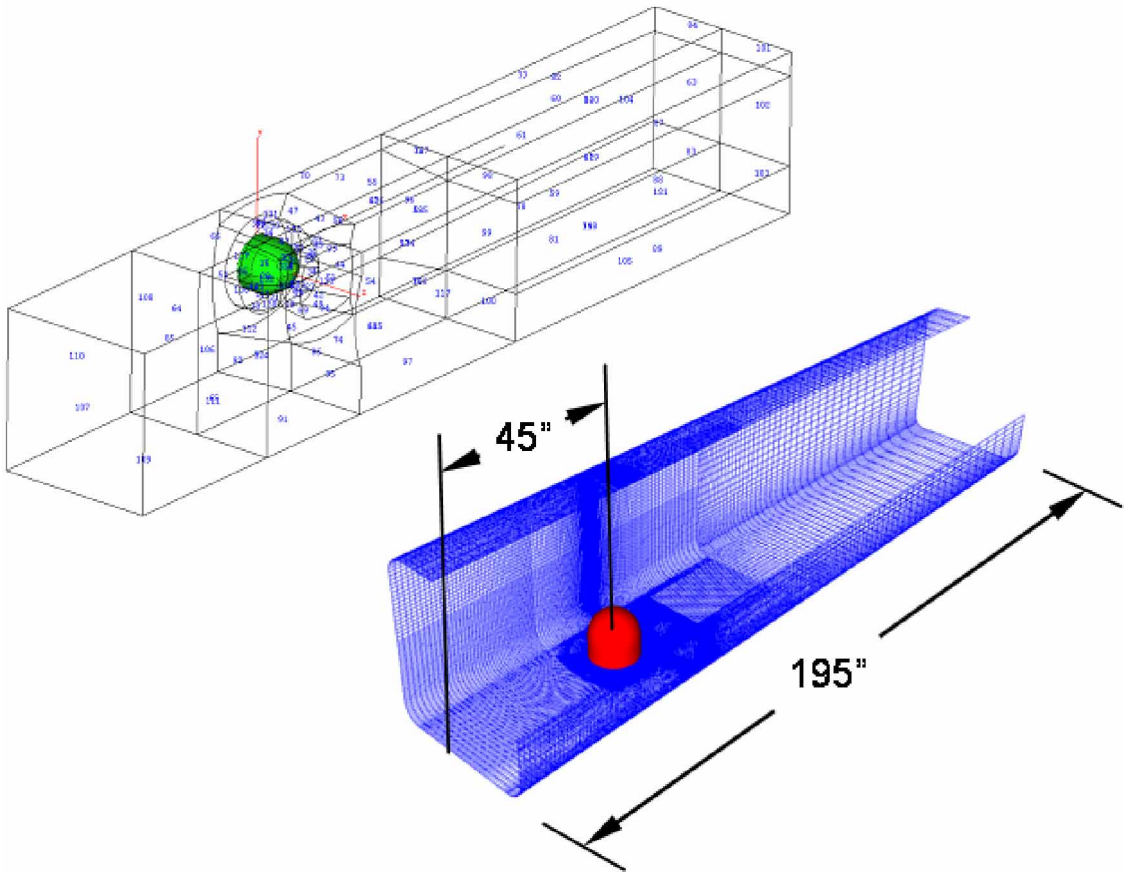

Fig. 17 Wind tunnel zones and total computational domain

5 CFD-BASED AERO-OPTICS MODEL

5.1 Computation grid

A multi-zone grid system was generated for the flow computation. The geometry was based on a computer aided design drawing looking downstream into the test section, as in Fig. 12. Figure 17 shows the resulting zones and computational domain. It extends 45 in (1.14 m) upstream of the turret centre to 150 in (3.81 m) downstream. A total of 2.7 million nodes divided into 52 zones were used. Figure 18 shows half of the computational grid in the vicinity of the turret. The blue grid represents the turret surface, the black grid defines the tunnel wall used as the base plane, and the red grid represents the central flow plane. To avoid degenerated cells at the top centre of the turret, a separate zone was added. The grid nodes were clustered near the turret surface and tunnel walls for the boundary layers. Grid cells were also clustered in the streamwise direction towards the downstream side of the turret, where separated shear layers were expected.

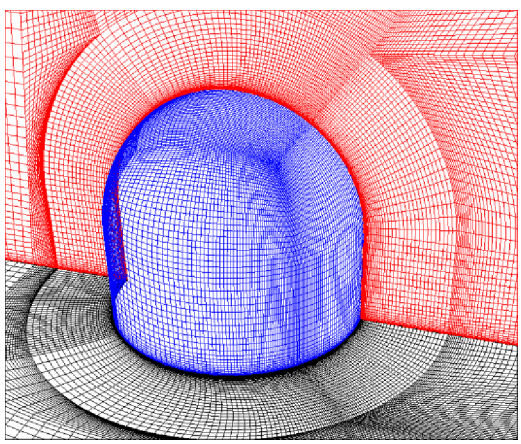

Fig. 18 Computational grid density in vicinity of turret

5.2 Flow solver and implementation of turbulence model

The flow solver uses a finite-volume technique with multi-zone method to solve the generalized multi-dimensional flow in a body-fitted grid system. The blending of density and pressure-based numerical methodology in the code allows efficient computation of both compressible and incompressible flow regimes. For time-accurate calculations, dual-time stepping was used. For turbulent flow computations,

the PANS technique was implemented in the k–ε turbulence model [**2**, **3**].

The PANS method uses two resolution-control parameters with filtering of the flow variables. In the traditional Reynolds-averaged Navier–Stokes (RANS) equations, turbulence is not resolved numerically, but modelled analytically to add turbulence effects to the mean flow. In the PANS approach, parameters are used to limit the unresolved scales to those smaller than the node separation, or cell size. The approach is similar to that used in large eddy simulation (LES). The difference is that LES uses wave number as the filter, whereas PANS uses turbulent kinetic energy and dissipation. The PANS parameters, ftk and fte, are defined as the ratio of the unresolved to the total turbulence kinetic energy and dissipation, respectively. Values range between 0 and 1; the smaller the value, the less turbulence scales are modelled and thus more directly computed. A zero value turns off the turbulence model, and solves like a direct numerical simulation. Unity value imposes a RANS model.

In theory, ftk and fte are functions of grid size and the distributions of total kinetic energy and dissipation. To simplify implementation in phase I of the programme, constant ftk and fte values were used throughout the computational domain. In phase II, the parameters were left as field variables varying from point-to-point. For the problem to remain computationally tractable, however, only two values of ftk were specified – one in free stream (ftk_1) and the other at the viscous surface (ftk_2). A smoothing function was applied between the two to avoid discontinuities. To further simplify the problem, fte was set to unity for all cases in which flow Reynolds numbers were high and turbulence dissipation scales not resolved.

5.3 Input conditions

The mach 0.4 dataset was used as the basis for validating the flow solution and aero-optics model. At the wind tunnel altitude of 7160 ft (2.18 km) above sea level, the M0.4 inflow velocity corresponds to 137 m/s with density 0.99 kg/m^3. The corresponding Reynolds number is 2.9×10^6.To simulate the boundary layer, the inlet flow was fitted with a velocity profile scaled from a 2005 wind tunnel boundary layer experimental survey [**1**]. Data at the $X = -27$ in (-68.6 cm) plane was scaled to the desired plane at $X = -45$ in, assuming an $X^{1/2}$ thickness growth rate. The measured and scaled profiles showed excellent agreement.

The unsteady nature of the flow requires time-dependent computation. However, a steady-state flow solution is computed initially to provide an initial condition for the unsteady flow computation. When the computation is switched to time-dependent, an induction period is required to transition to the unsteady solution. The time-accurate flow computation requires a small time increment to converge at each step. In this analysis, the highest frequency is ~2000 Hz, or a period of 500 μs. To ensure accuracy, 5 μs time steps were used. Each case was run for more than 5000 steps (25 ms total duration) before data collection. Solutions were saved at 50 μs intervals. A total duration of 15 ms (300 frames) of data was stored for the wavefront statistics supporting validation.

As mentioned, the PANS flow model uses two ftk parameters. Figure 19 shows the distribution of ftk_1 (freestream) and ftk_2 (wall or boundary) in the flowfield. If the two values are the same, ftk is constant throughout the domain. If they vary, there is a smooth transition. A number of ftk pairs were traded to evaluate the effects to determine the combination that best satisfies the required flow features such as, well-resolved vortices in the shear layer and separation point. Results of ftk = ftk_1–ftk_2 = 0.4–1.0 (case 1) and ftk = 0.5 (case 2) are reported. In case 2, the flow model is equivalent to that used in phase I. The approach also serves to verify the utility of the PANS upgrade.

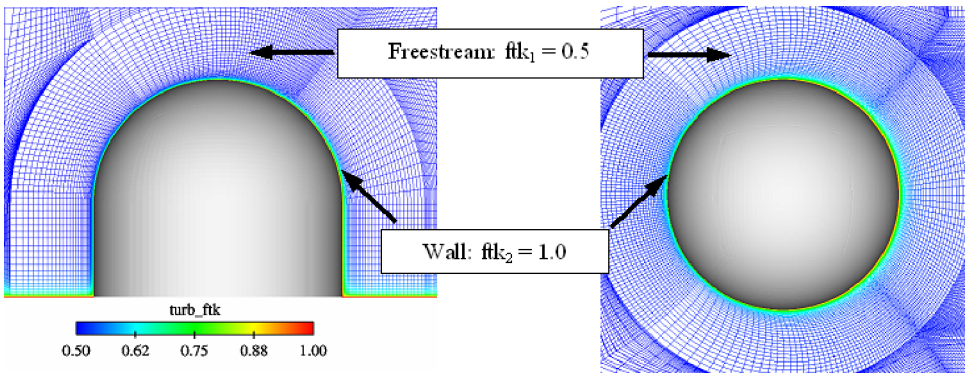

Fig. 19 Distributions of ftk about turret

6 COMPARISON OF FLOW SOLUTIONS AND FLUID MEASUREMENTS

An instantaneous realization of the pressure contour in two perpendicular plane sections for cases 1 and 2 is shown in Fig. 20. The left plot in each is a vertical section through the central $Y = 0$ plane. The right plot is a horizontal section through the shoulder ($Z = 4.5$ in $= 11.4$ cm) plane. The low pressure region behind the turret is as a result of the large wake. In the left-hand figures, a low pressure circular area forward of the turret base is the core of the horseshoe (or necklace) vortex. The flow separates from the surface and a shear layer starts to form at 100 to 110° elevation. The instability in the shear layer causes the flow to roll into vortices. When viewed as a function of time at 1000 samples (or frames) per second, the pressure within the vortices exhibits the oscillatory behaviour observed in particle image velocimetry. This is the most distinctive and prominent feature critical to an accurate simulation of the aero-optical effect. The two perpendicular views show a significant number of vortices formed aft of the cylindrical base and dome. More vortices occur in case 2.

Figures 21 and 22 compare the velocity profile measurements with those extracted from flow solutions at locations no. 1 and no. 4, respectively. The hot-wire locations are defined in Fig. 14. The red and green curves represent cases 1 and 2 predictions with blue points representing measurements. Since the hot wire was parallel to the Y-axis in the wind tunnel, the magnitude of the velocity was calculated by using the U and W components only. The mean velocity is shown on the left in each figure, with rms fluctuation on the right. Both are normalized with respect to the inflow condition because M0.35 data were used

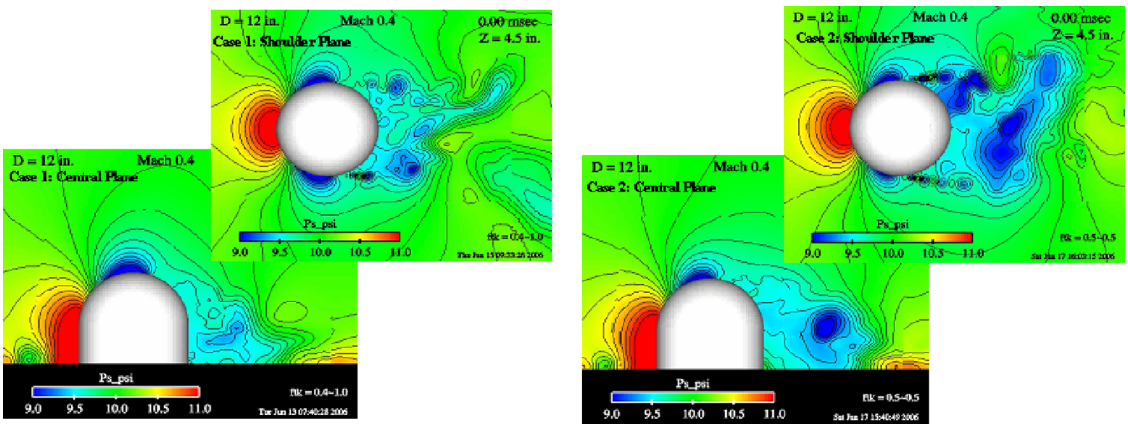

Fig. 20 Case 1 (ftk1 = 0.4, ftk2 = 1.0) and case 2 (ftk1 = ftk2 = 0.5) pressure contour realization in the central and shoulder plane sections

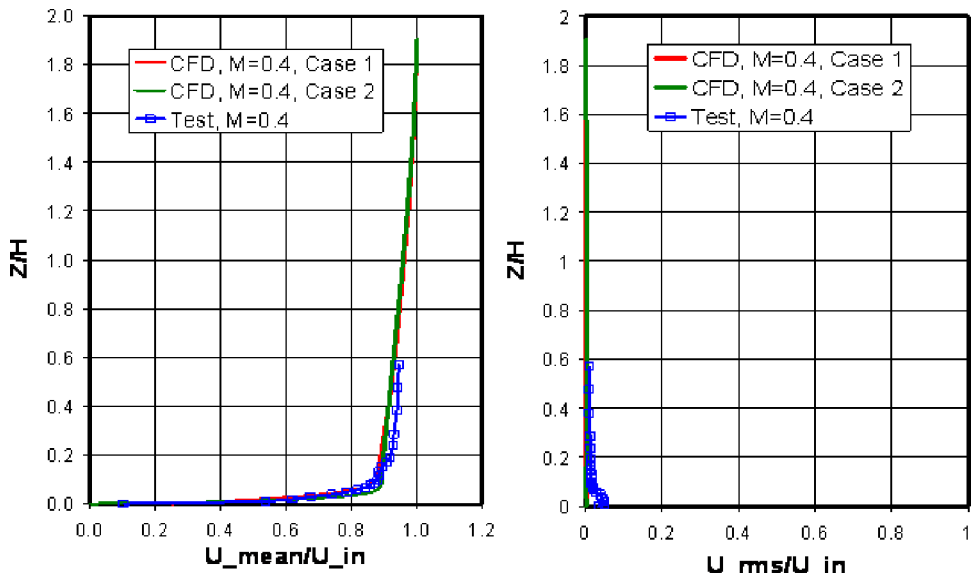

Fig. 21 Predicted and measured mean (normalized) and rms velocity profiles at location 4

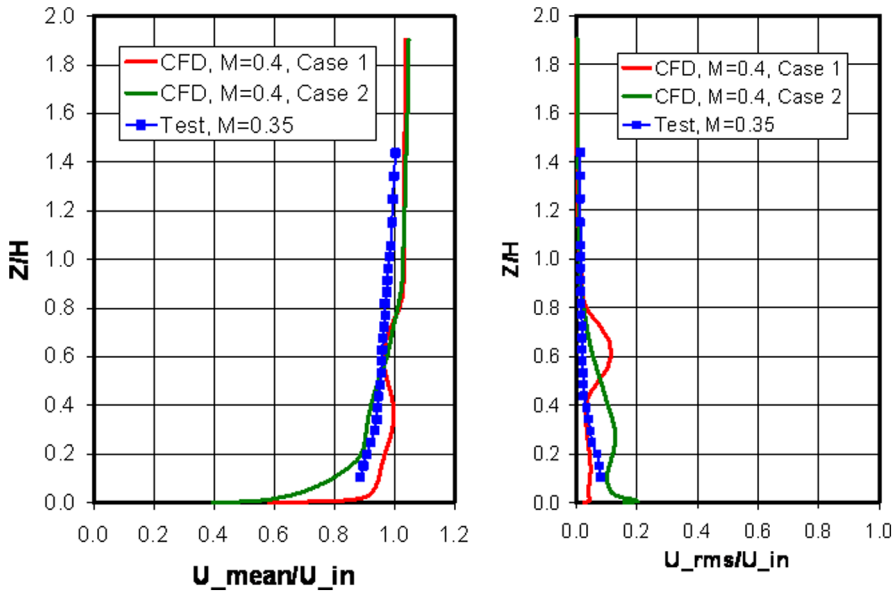

Fig. 22 Predicted and measured mean (normalized) and rms velocity profiles at location 4

at locations no. 2 to no. 4, where no mach 0.4 data were available. The vertical axis is the distance from the base plane (Z-axis) normalized to the turret height (H) of 10.5 in (26.7 cm).

At location no. 1, 17 in (43.2 cm) upstream of turret centre, both solutions show a boundary layer profile characteristic of a flat plate. The case 1 predicted profile shows a boundary layer thickness of $Z/H = 0.1$, which matches the test data. Case 2 has a thinner boundary layer with a normalized thickness of only 0.07. The RMS values for both test and prediction are very low, as expected for flow over a flat plate. Location no. 4 (Fig. 22) is downstream of the turret in the middle of the wake. The wake in case 1 is nearly closed.

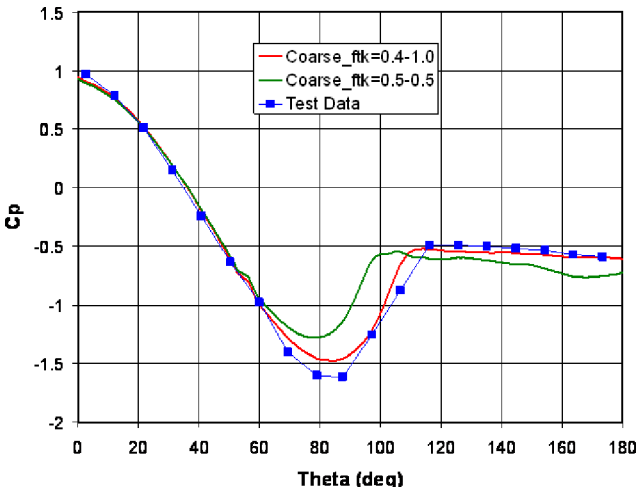

Fig. 23 Comparison of test measurement and CFD-based prediction for static pressure coefficient

Figure 23 shows the time-averaged pressure coefficient (C_P) on the hemisphere surface, as a function of elevation angle. The pressure drops along the streamline on the windward side, but recovers on the leeward side until flow separates. A wake is formed after separation, with pressure fluctuating around the separation pressure. The test data show separation at ∼115°. The CFD shows separation at ∼110° and 100° for cases 1 and 2, respectively. The error in the predicted angle is the result of the upgraded flow model. The case 1 prediction is closer due to the full RANS (ftk = 1.0) estimate inside the boundary layer.

7 OPTICAL PATH DIFFERENCE

The OPD or WFE computed from the CFD analysis is based on sampling the flow solution within a 25 × 25 array of 'beamlets' extending from the surface of the turret to the tunnel wall, as shown in Fig. 24. The parallel-piped close packed array is co-aligned with the LOS beam. The computed density field is interpolated to the beam grid for each frame in the solution. The density is summed along each beamlet ray and converted to optical path length (OPL), by using the Gladstone–Dale equation. The composite wavefront, formed by the OPL in each beamlet, is processed over the same aperture diameter as the Hartmann wavefront data described above.

Instantaneous realizations of the tilt-removed OPD maps at 120° and 132° for cases 1 and 2 are shown in Figs 25 and 26. These are the CFD equivalents of the reconstructed wavefronts from the measurements in Fig. 16. Although direct comparison of the random realizations is not possible, characteristic scales in the

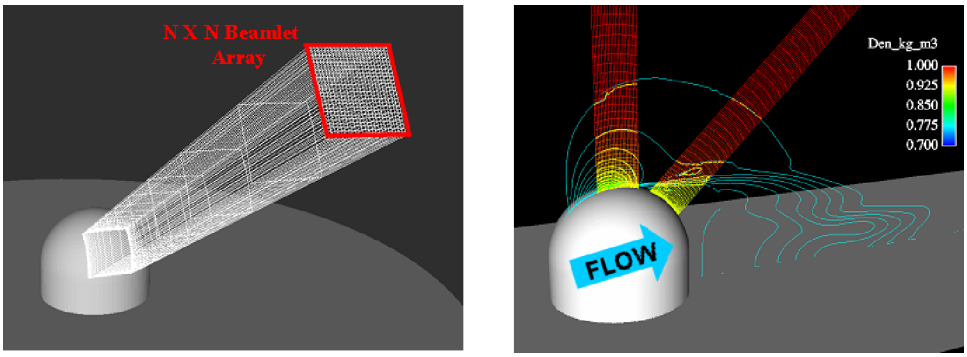

Fig. 24 Beamlet array (left) for OPD modelling and defining LOS (right). LOS angle is defined in elevation with 0° into the flow

wavefronts (at 132°) are similar. As expected from the flow solution, case 1 produces a smaller OPD than case 2.

8 WIND TUNNEL DATA AND CFD-BASED MODEL COMPARISON

Two FOMs are used to compare the measured and CFD-based wavefronts. The first is rms WFE, defined as the aperture-averaged standard deviation of the wavefront phase (φ) with piston and tilt removed. These are averaged over time (or ensemble), i.e.

$$\text{RMS OPD}, \sigma_{\text{rms}} = [\langle \text{E}\{\varphi^2(r,t)\} - \{\text{E}\{\varphi(r,t)\}\}^2 \rangle]^{1/2}$$

where $< \ldots >$ denotes time average and $\text{E}\{\ldots\}$ = expectation value $= \iint \varphi(r,t)\text{d}r / \iint \text{d}r$.

In this analysis, the OPD is calculated over the central 4.5 in (11.4 cm) of the 5 in (12.7 cm) diameter beam.

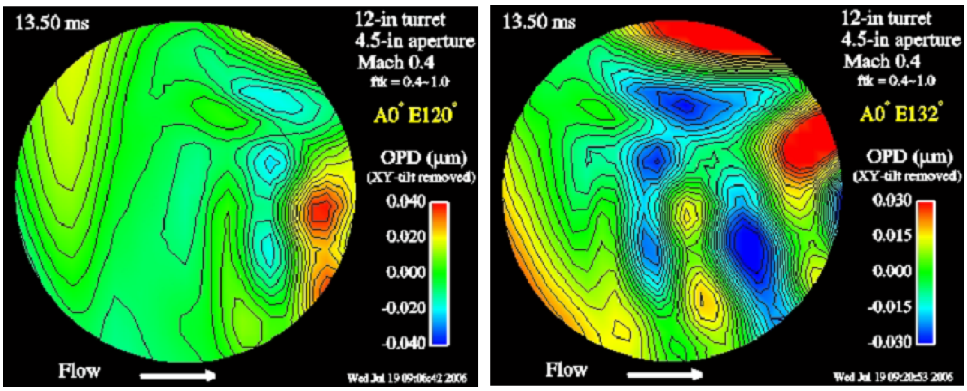

Fig. 25 Case 1 tilt-removed OPD realization at 120° and 132° elevations

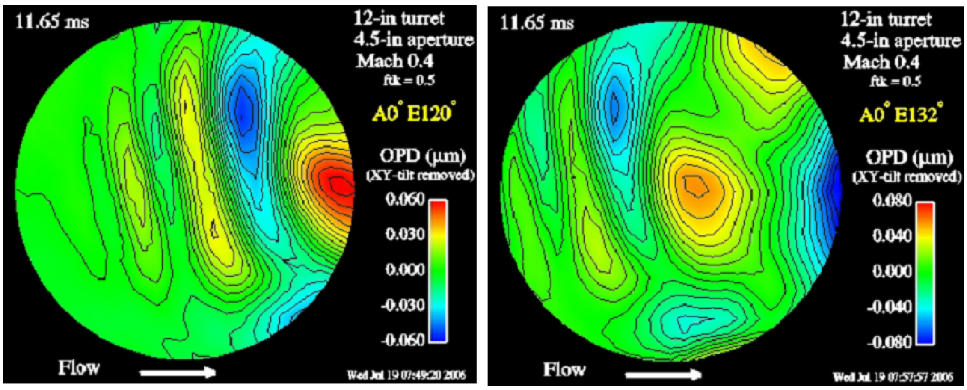

Fig. 26 Case 2 tilt-removed OPD realization at 120° and 132° elevations

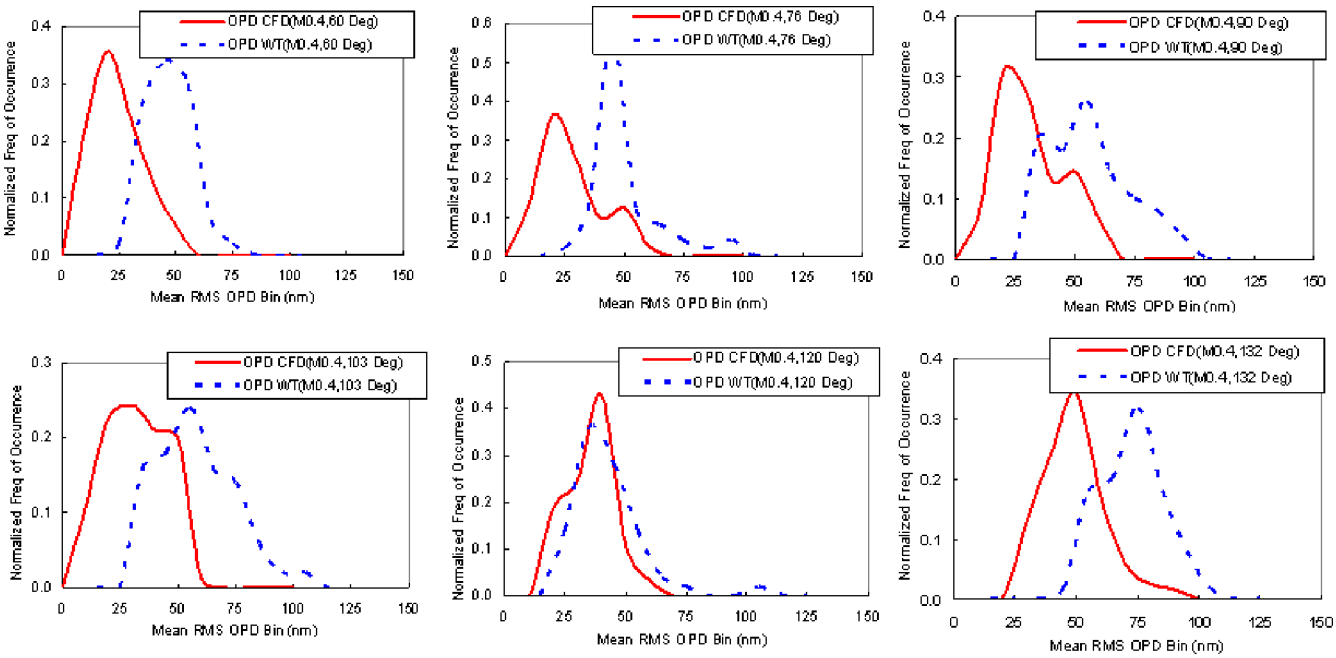

Fig. 27 OPD probability density functions for two-dimensional WFS measurements (blue) and CFD model (red, case 2) for elevation angles of 60°, 76°, 90°, 103°, 120°, and 132°

The second FOM is the ensemble-averaged phase correlation length L_c based on the first zero crossing of the autocorrelation $[R_{\varphi\varphi}(\Delta r)]$ of the phase along the flow direction

$$R_{\varphi\varphi}(\Delta r) = \langle \varphi(r,t)\varphi(r+\Delta r,t)\rangle / \langle \varphi^2(r,t)\rangle$$

Probability density functions (PDFs) for the M0.4 Hartmann (blue) and CFD-based (red) OPDs are shown in Fig. 27. Note the units of OPD are in nm. Figure 28 shows mean values as a function of elevation angle. The PDFs are based on 300 samples at each angle. The results show good agreement throughout the elevation range. Also, the expected trend in OPD for the two limiting cases described in the Phase I results is shown in Fig. 28. The lower boundary assumes the OPD increases as $1/\sin\theta_{\text{elev}}$ for a turbulent shear layer of constant thickness. The upper boundary assumes an increase with angle of incidence and 10° shear layer divergence. The value 10° was estimated from CFD-based flow solutions and wind tunnel flow visualization. The two limits fall between the wind tunnel measurements and CFD predictions. Thus, not only do the measurements and model show reasonable agreement, but they are consistent with observations.

PDFs were also calculated for the phase correlation length. The same correlation function and correlation length criterion were used for the wind tunnel and CFD-based data. The PDFs as a function of elevation angle are shown in Fig. 29. Agreement is excellent between measurement and prediction. Figure 30 shows the mean values and standard deviation of the

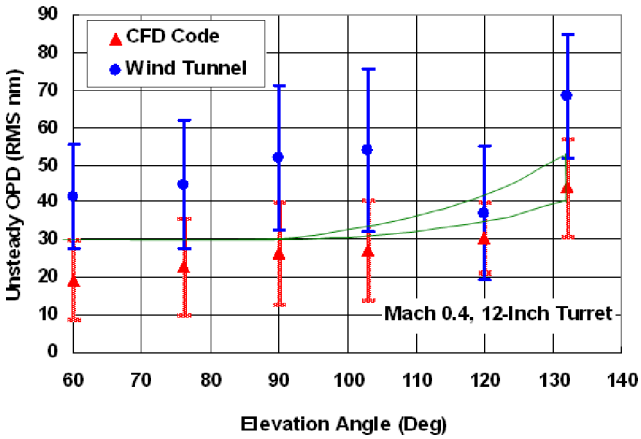

Fig. 28 Mean and standard deviation of OPD for wind tunnel measurements (blue) and CFD (red, case 2) model

correlation length as a function of elevation. Note that the correlation length does not change much with elevation. As the elevation increases beyond 90° with respect to flow heading, the correlation length viewed normal to the LOS is reduced by a factor of $\sin\theta_{\text{elev}}$. However, scale lengths further back in the wake, and thus with elevation, tend to increase. This can be seen in the pressure contours generated in the flow solution. The results of both measurement and prediction indicate that the two effects nearly cancel over the range of elevation and flow conditions. Consistency between the CFD-based model and measurements support this conclusion.

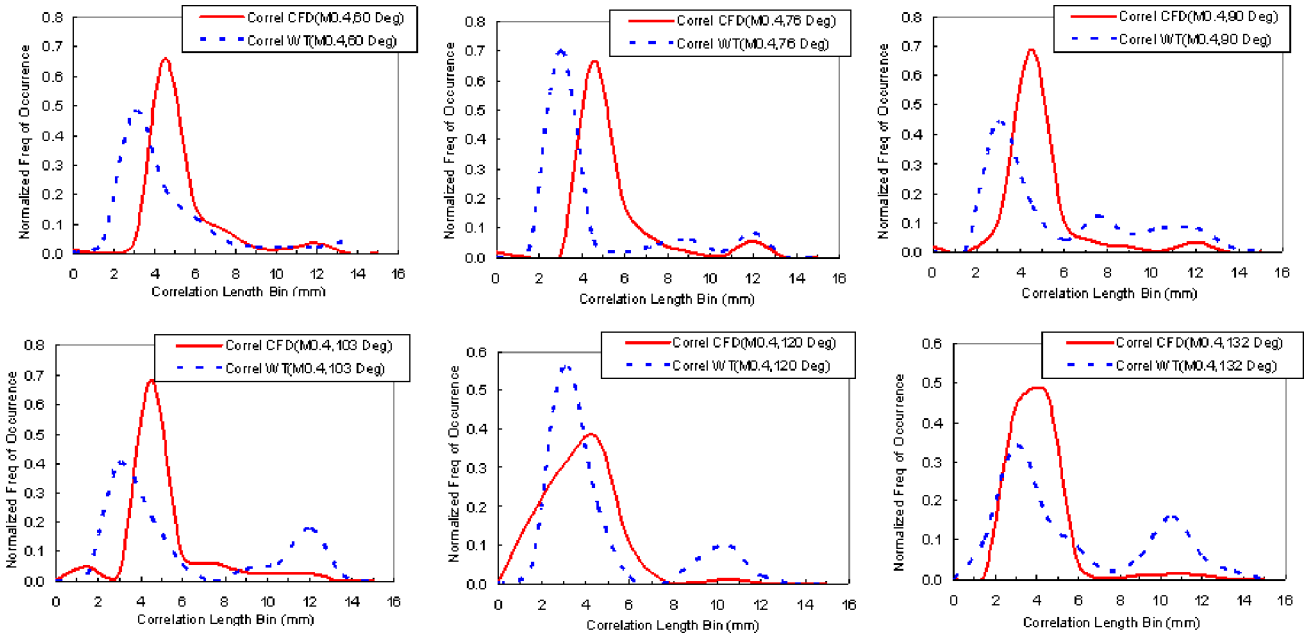

Fig. 29 Phase correlation length PDFs for WFS measurements (blue) and CFD model (red, case 2) for elevation angles of 60°, 76°, 90°, 103°, 120°, and 132°

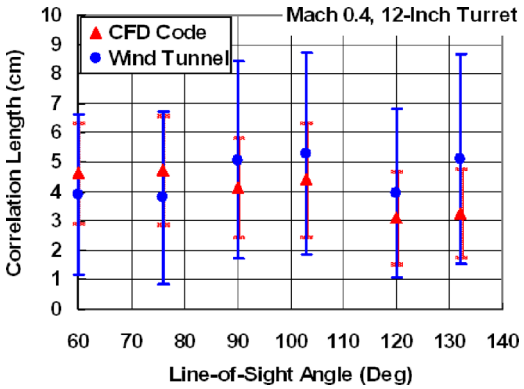

Fig. 30 Mean and standard deviation of phase correlation length for wind tunnel measurements (blue) and CFD (red, case 2) model

9 SUMMARY AND CONCLUSIONS

A CFD-based aero-optics phase model has been validated by using WFS measurements in a subsonic wind tunnel experiment. The model was based on the same wind tunnel and turret configuration and dimensions, and flow conditions.

After developing system requirements, establishing the trade space, and defining the FOMs, a 12 in diameter optical turret was fabricated. In parallel with the hardware development and initial test data, limitations of the CFD code were identified, and appropriate updates were made to the flow physics to properly model spatial and temporal frequency characteristics, including necklace vortex structure and separation point location. This was followed by a series of WFS tests, showing good agreement between predicted and measured statistics of the optical wavefronts.

REFERENCES

1 **Dumas, J., Fuqua, M.,** and **Hayden, T.** Final report: boundary layer survey of the subsonic wind tunnel. Department of Aeronautics, United States Air Force Academy, May 2005.

2 **Girimaji, S. S.** and **Abdol-Hamid, K. S.** Partially-averaged Navier Stokes model for turbulence: implementation and validation. In Proceedings of the 43rd AIAA Aerospace Sciences Meeting, Hybrid RANS/LES & Other Unsteady Models, Reno, Nevada, 10–13 January 2005, AIAA paper 2005-502.

3 **Tosh, A., Frendi, A.,** and **Girimaji, S.** Partially averaged Navier Stokes: a new turbulence model for unsteady flows with application to acoustics. In Proceedings of the 11th AIAA/CEAS Aeroacoustics Conference, Monterey, California, USA, 23–25 May 2005, AIAA paper 2005-2987.

APPENDIX

Notation

C_p	static pressure coefficient
E{...}	expectation value operator
fte	turbulence dissipation parameter
ftk_1	freestream turbulence kinetic energy parameter

ftk_2	wall or boundary turbulence kinetic energy parameter
L_c	phase correlation length
LOS	line-of-sight
M	mach number
$R_{\varphi\varphi}(\Delta r)$	autocorrelation function of phase φ at separation value Δr
U, V, W	X-, Y-, and Z-axis components of velocity
$\kappa{-}\varepsilon$	kappa-epsilon turbulence model
σ_{rms}	aperture-average RMS WFE
$\varphi(r,t)$	optical phase in $x, y; t$
$< \ldots >$	ensemble time-average